Supplementary Information

for paper

Novel bimetallic Ln^{III}/V^{IV} (Ln = Gd, Tb, Dy, Er, Yb, Lu) compounds based on cyclopropane-1,1-dicarboxylate anions and bulky tetrabutylammonium cations: synthesis, structure, magnetic properties, and thermal decomposition

Evgeniya S. Bazhina, *[a] Maxim A. Shmelev, [a] Natalia V. Gogoleva, [a] Anna K. Matiukhina, [a] Pavel N. Vasilyev, [a] Nikolay N. Efimov, [a] Mikhail A. Kiskin, [a] and Igor L. Eremenko [a]

[a] *N. S. Kurnakov Institute of General and Inorganic Chemistry of the Russian Academy of Sciences, Leninsky prosp. 31, Moscow 119991, Russian Federation*

[*] *E-mail: bazhina@igic.ras.ru*

Description of the crystal structures

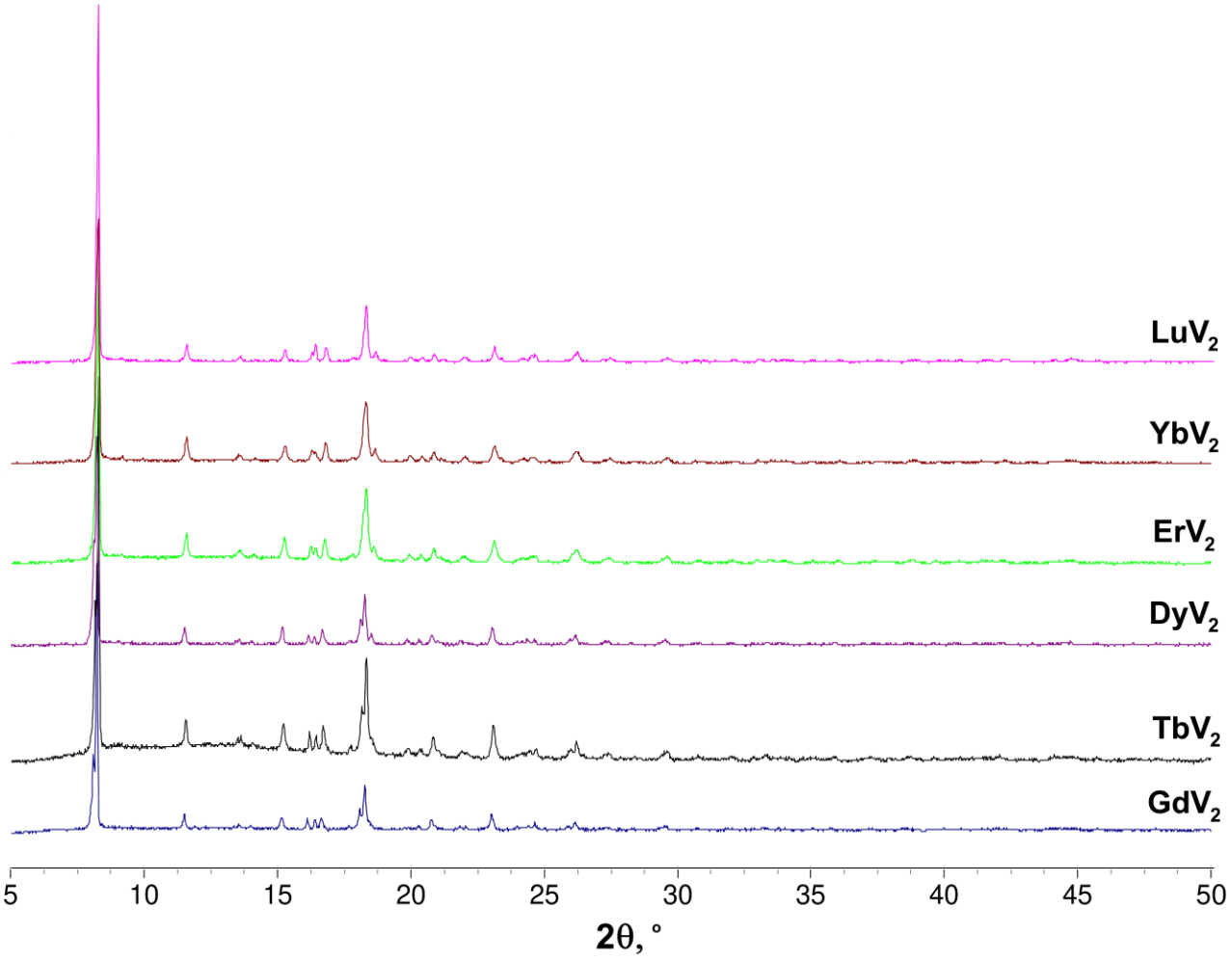

Figure S1. Experimental powder XRD patterns for compounds **LnV_2** (2θ range of 5-50°).

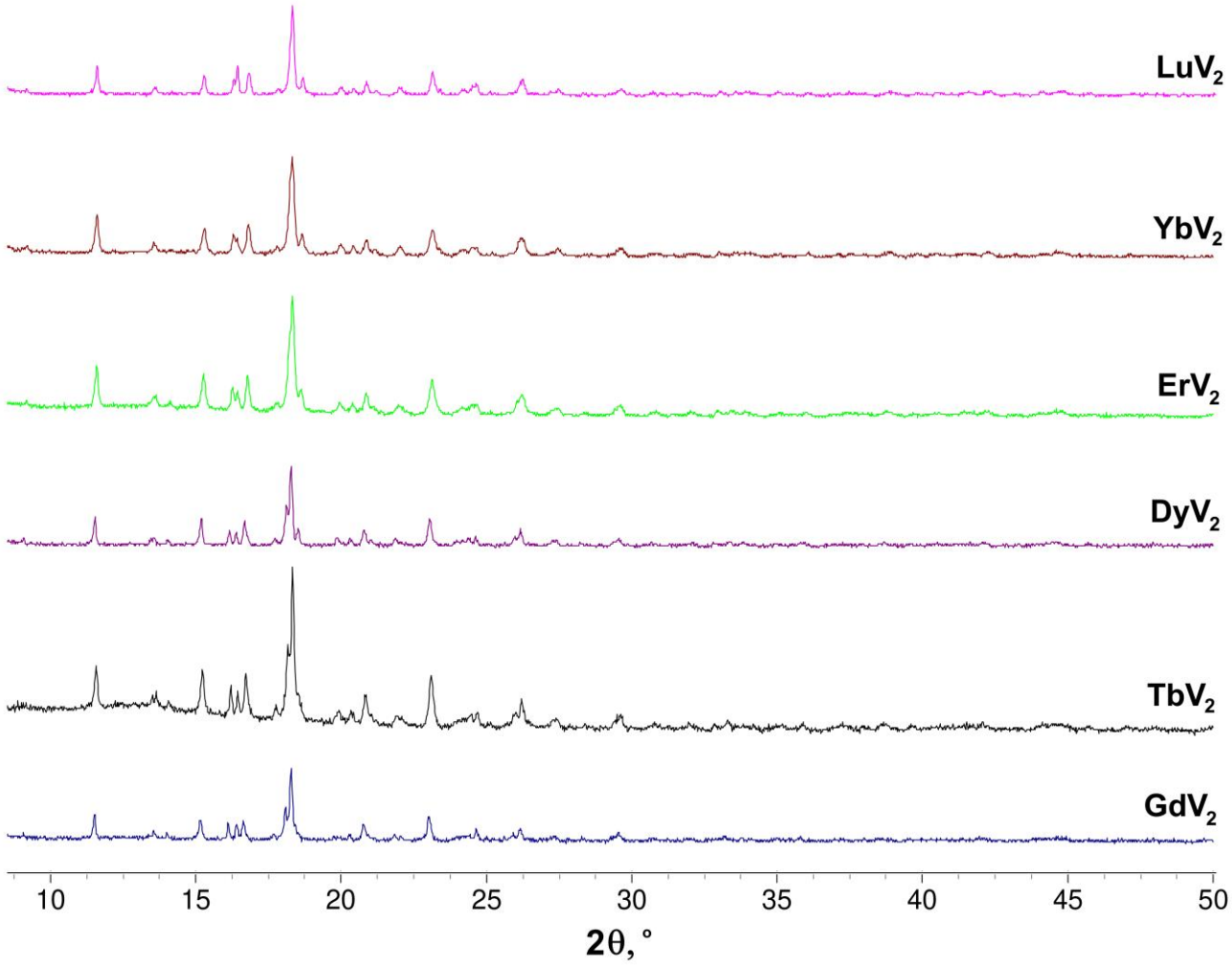

Figure S2. Experimental powder XRD patterns for compounds **LnV_2** (2θ range of 10-50°).

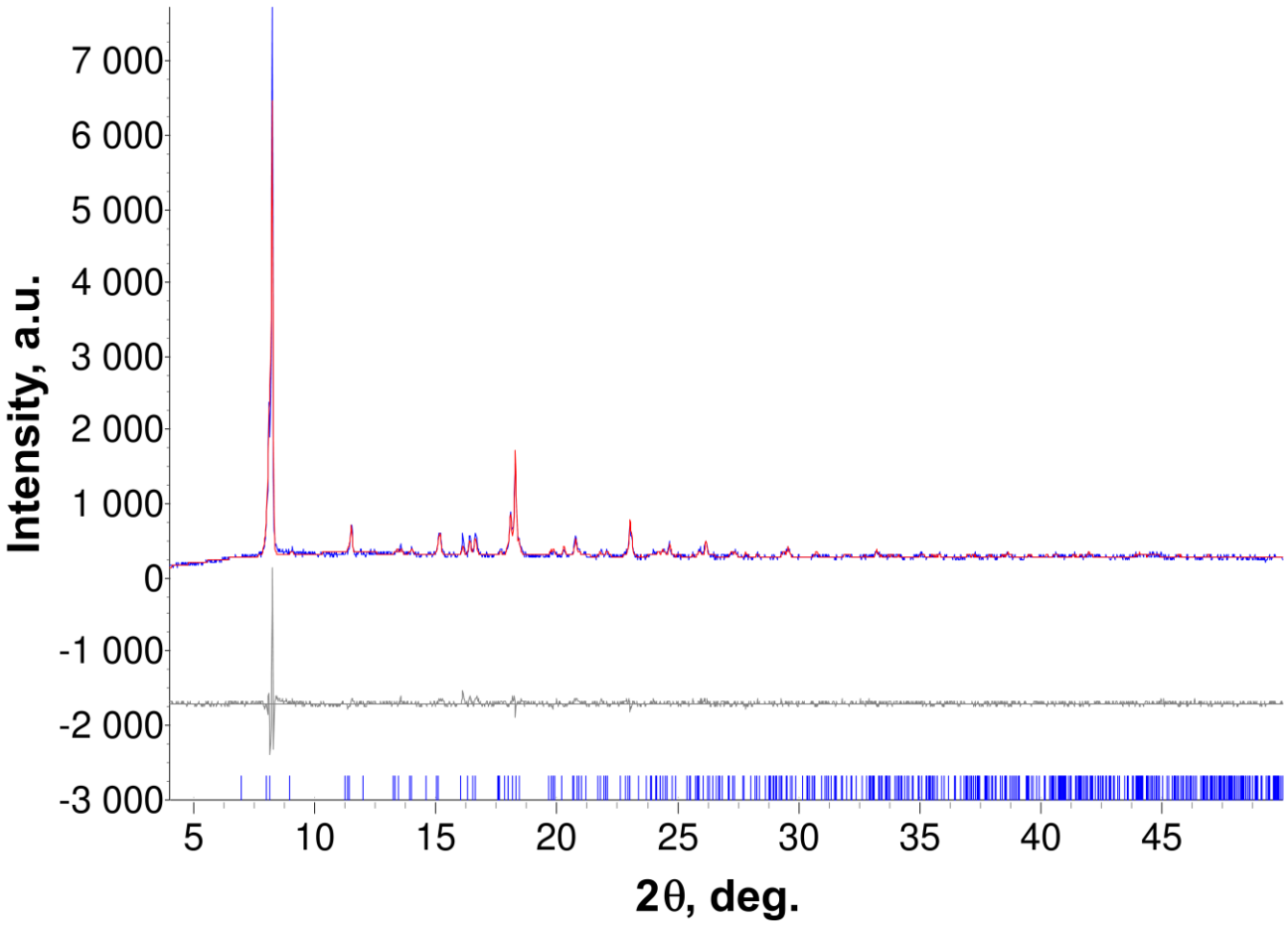

Figure S3. The experimental (blue line) and calculated (red line) powder XRD patterns for **GdV_2** and their difference (grey line). The SCXRD data for **GdV_2** was used to simulate the theoretical line. Blue ticks indicate calculated positions of the reflections.

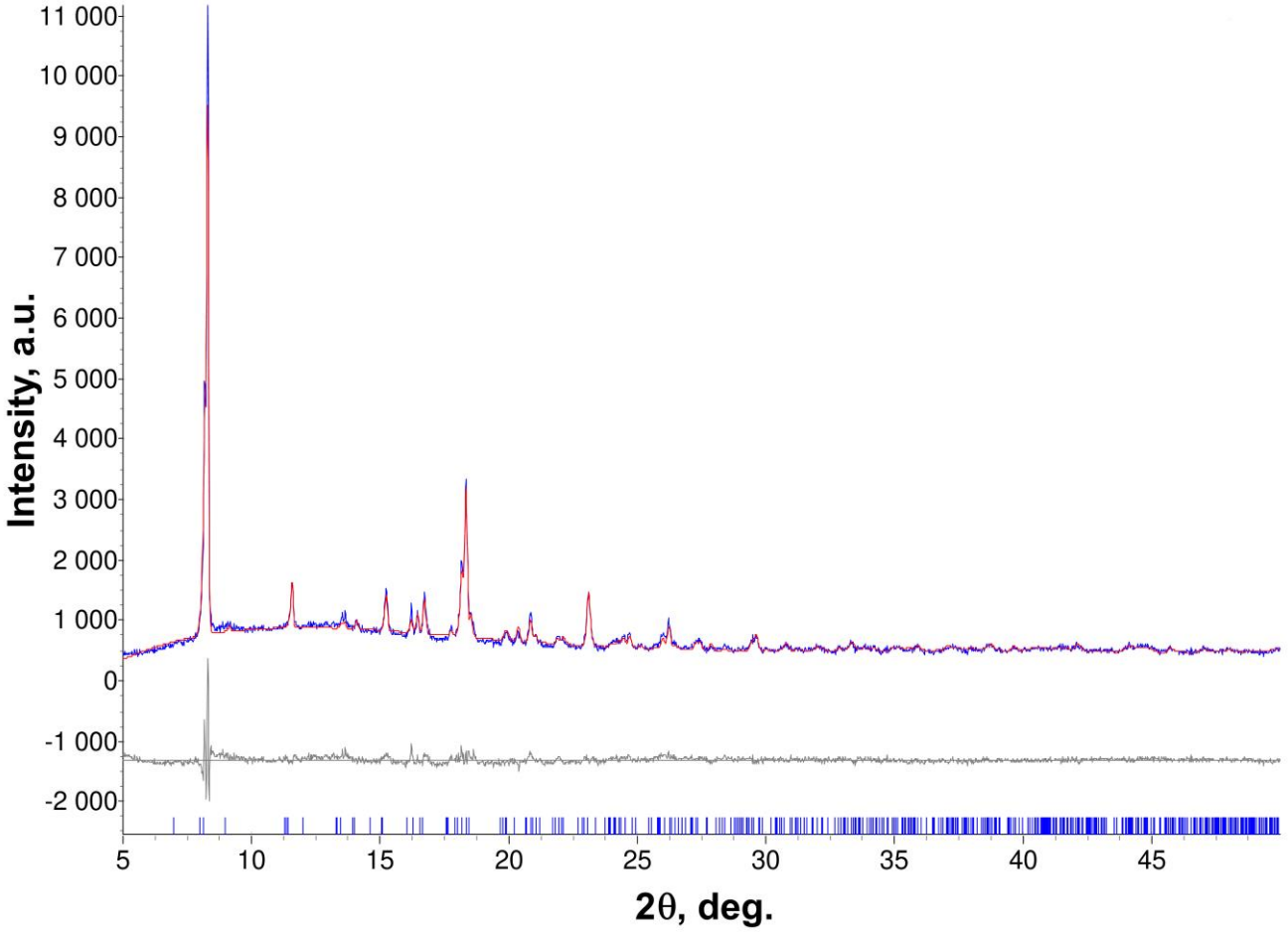

Figure S4. The experimental (blue line) and calculated (red line) powder XRD patterns for **TbV_2** and their difference (grey line). The SCXRD data for **TbV_2** was used to simulate the theoretical line. Blue ticks indicate calculated positions of the reflections.

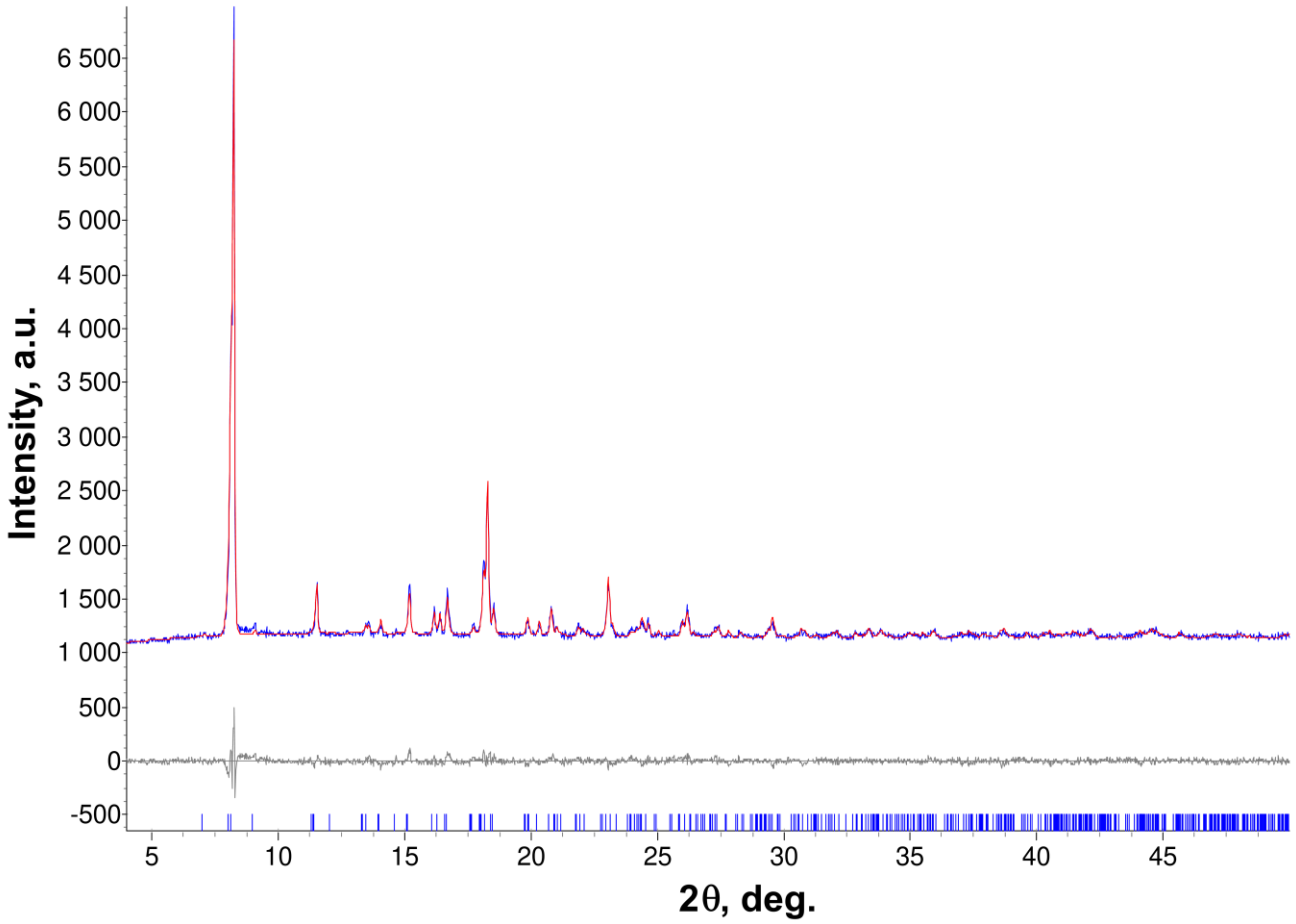

Figure S5. The experimental (blue line) and calculated (red line) powder XRD patterns for **DyV_2** and their difference (grey line). The SCXRD data for **DyV_2** was used to simulate the theoretical line. Blue ticks indicate calculated positions of the reflections.

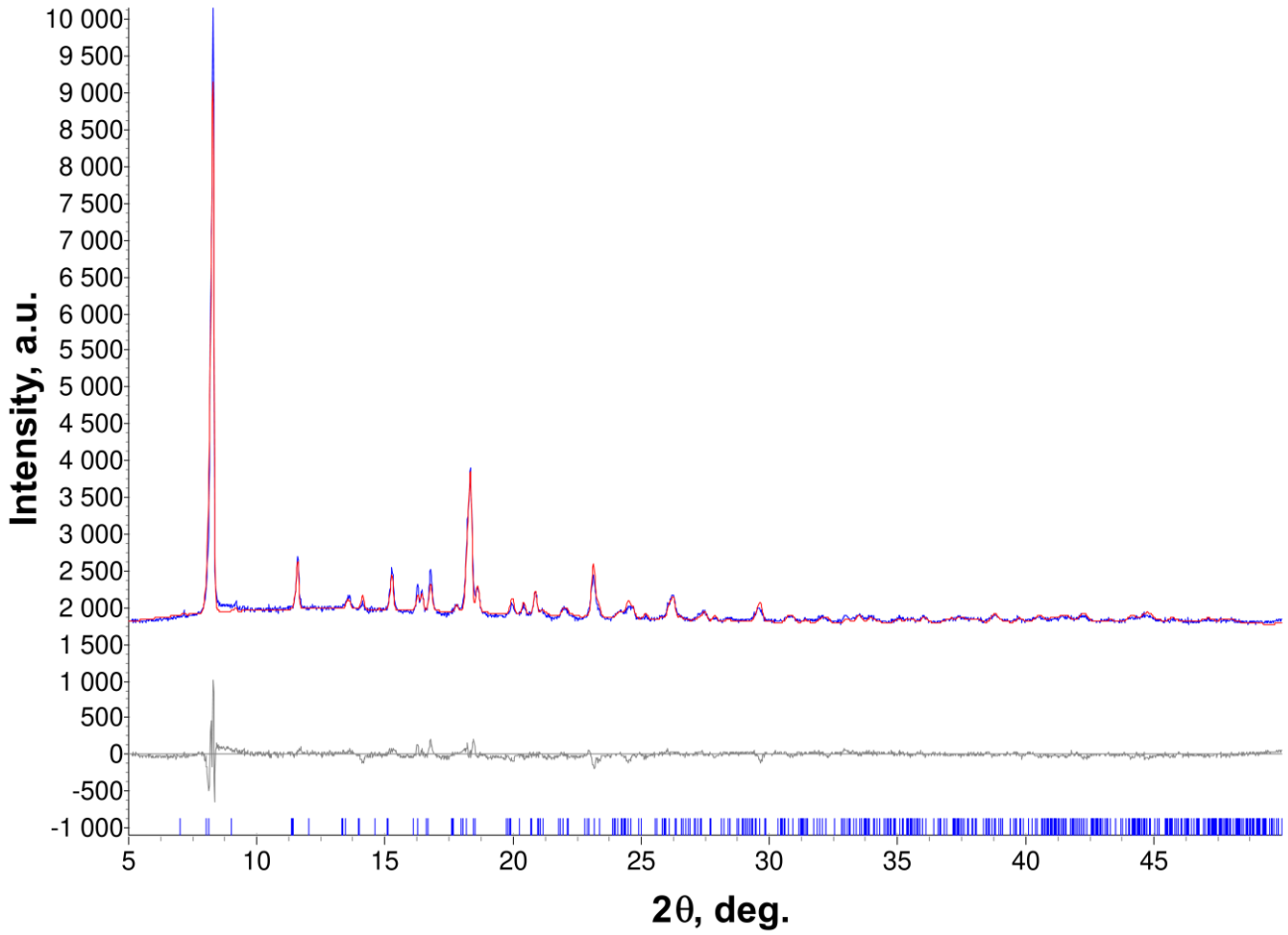

Figure S6. The experimental (blue line) and calculated (red line) powder XRD patterns for **ErV_2** and their difference (grey line). The SCXRD data for **DyV_2** was used to simulate the theoretical line. Blue ticks indicate calculated positions of the reflections.

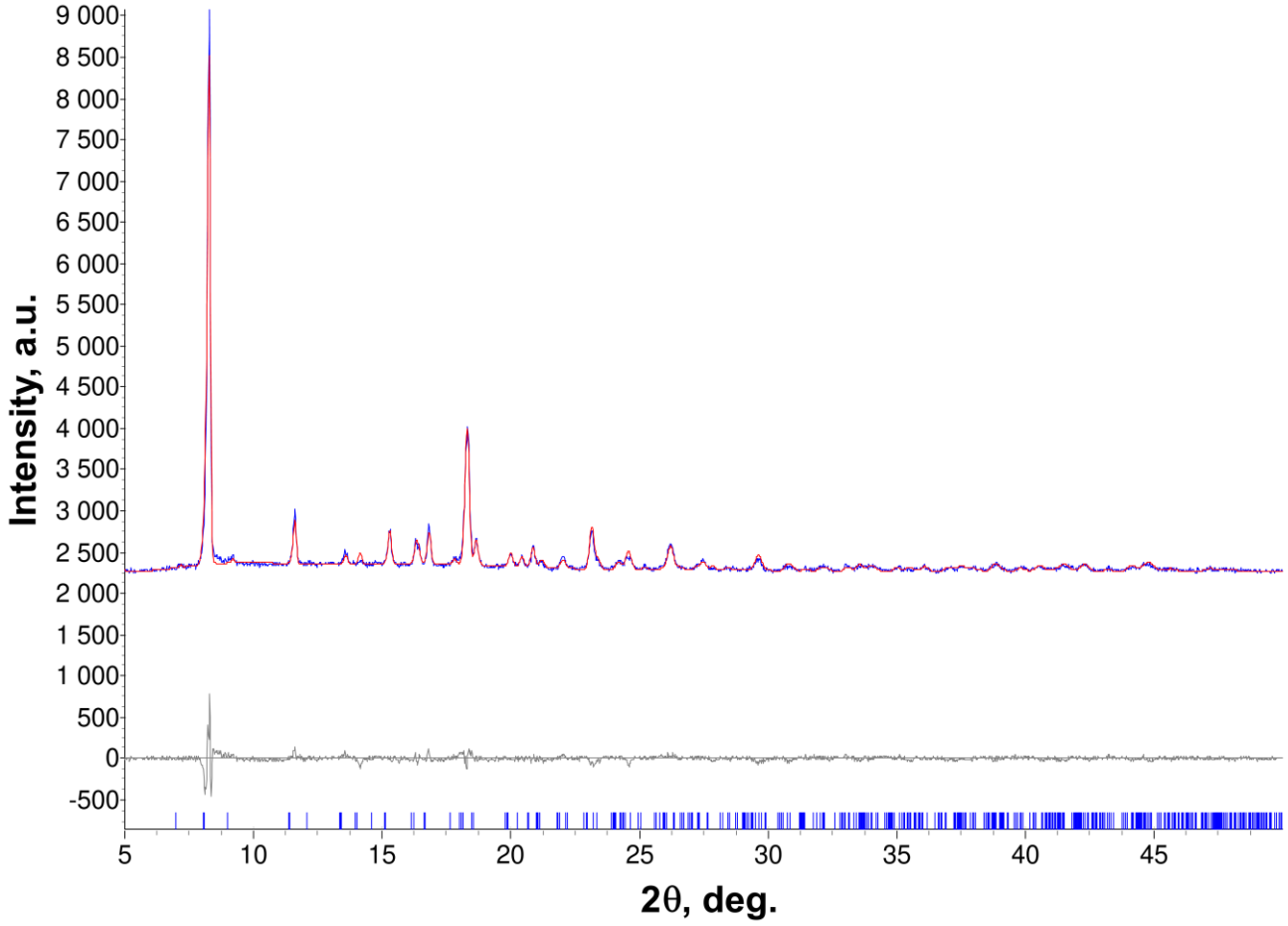

Figure S7. The experimental (blue line) and calculated (red line) powder XRD patterns for **YbV$_2$** and their difference (grey line). The SCXRD data for **DyV$_2$** was used to simulate the theoretical line. Blue ticks indicate calculated positions of the reflections.

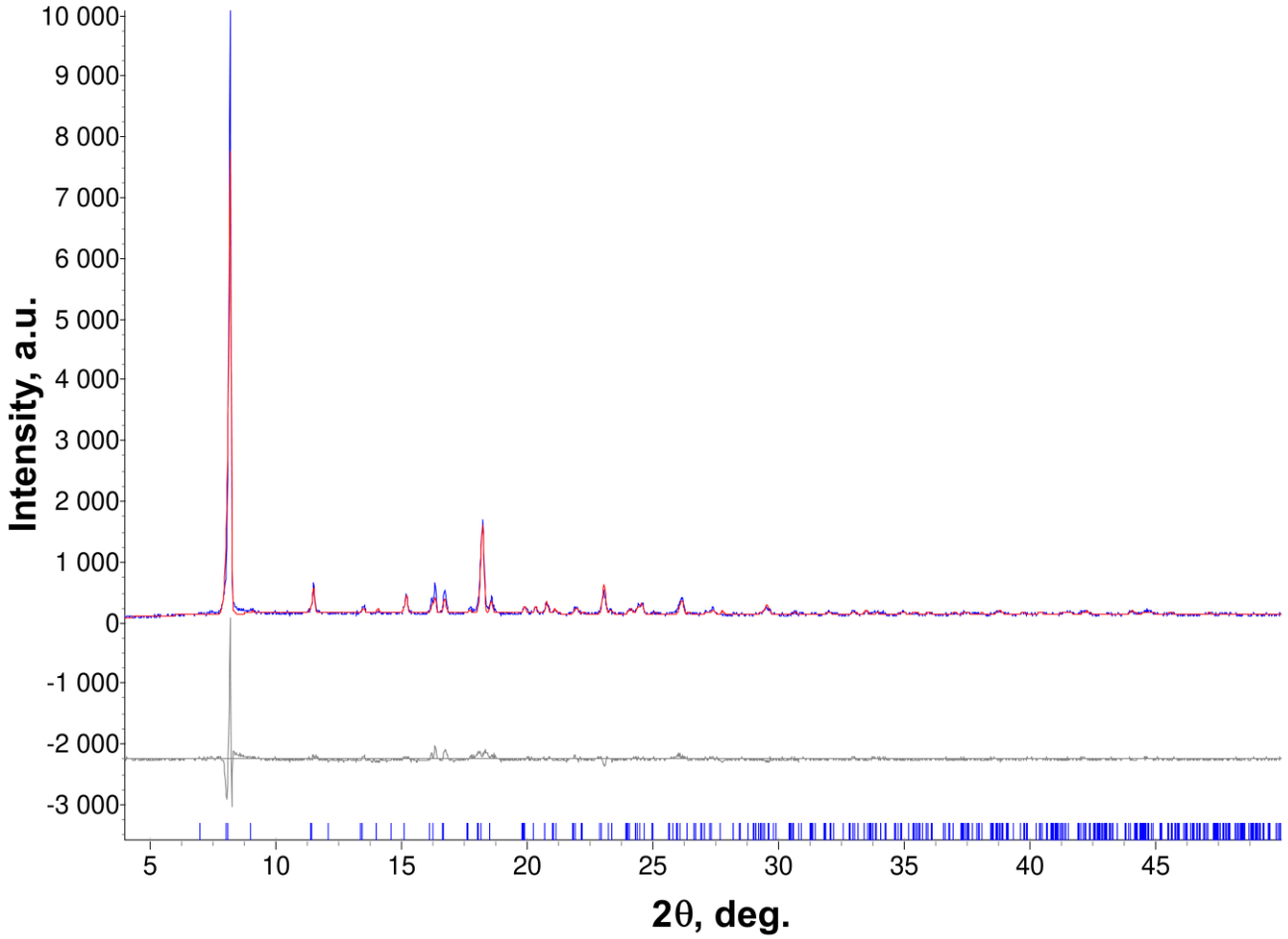

Figure S8. The experimental (blue line) and calculated (red line) powder XRD patterns for **LuV_2** and their difference (grey line). The SCXRD data for **DyV_2** was used to simulate the theoretical line. Blue ticks indicate calculated positions of the reflections.

Table S1. Continuous Shape Measures (CShM) for GdO_8, TbO_8 and DyO_8 coordination polyhedra in compounds **GdV_2**, **TbV_2**, and **DyV_2**. The lowest CShM values are highlighted, indicating the best fits.

Structure ML_8	**SAPR-8**	**TDD-8**	**JBTPR-8**	**BTPR-8**	**JSD-8**
GdV_2	**0.297**	1.879	2.783	2.203	4.820
TbV_2	**0.346**	1.876	2.868	2.259	4.934
DyV_2	**0.320**	1.860	2.837	2.233	4.892

Codes: SAPR-8 (D_{4d}) Square antiprism; TDD-8 (D_{2d}) Triangular dodecahedron; JBTPR-8 (C_{2v}) Biaugmented trigonal prism J50; BTPR-8 (C_{2v}) Biaugmented trigonal prism; JSD-8 (D_{2d}) Snub disphenoid J84.

Table S2. Selected bond angles (ω, deg.) for **GdV_2**.

Angle	ω	Angle	ω
O11–Gd1–O11$^{(i)}$	137.8(2)	O14$^{(i)}$–Gd1–O13	111.01(14)
O11$^{(i)}$–Gd1–O14$^{(i)}$	76.50(14)	O14–Gd1–O13	141.41(14)
O11–Gd1–O14$^{(i)}$	72.06(14)	O14–Gd1–O13$^{(i)}$	111.00(14)
O11$^{(i)}$–Gd1–O14	72.06(14)	O14$^{(i)}$–Gd1–O13$^{(i)}$	141.41(14)
O11–Gd1–O14	76.50(14)	O14$^{(i)}$–Gd1–O12$^{(i)}$	144.11(14)
O11–Gd1–O13	74.17(14)	O14–Gd1–O12$^{(i)}$	70.95(14)
O11$^{(i)}$–Gd1–O13	145.03(14)	O14–Gd1–O12	144.12(14)
O11–Gd1–O13$^{(i)}$	145.03(14)	O14$^{(i)}$–Gd1–O12	70.95(14)
O11$^{(i)}$–Gd1–O13$^{(i)}$	74.17(14)	O13–Gd1–O13$^{(i)}$	81.3(2)
O11$^{(i)}$–Gd1–O12$^{(i)}$	115.69(14)	O13–Gd1–O12$^{(i)}$	78.98(14)
O11$^{(i)}$–Gd1–O12	78.37(14)	O13–Gd1–O12	72.70(14)
O11–Gd1–O12	115.69(14)	O13$^{(i)}$–Gd1–O12$^{(i)}$	72.70(14)
O11–Gd1–O12$^{(i)}$	78.37(14)	O13$^{(i)}$–Gd1–O12	78.98(14)
O14–Gd1–O14$^{(i)}$	82.6(2)	O12$^{(i)}$–Gd1–O12	142.4(2)

Symmetry code: (i) *x*, -*y*+3/2, -*z*+1/2.

Table S3. Selected bond angles (ω, deg.) for **TbV_2**.

Angle	ω	Angle	ω
O11–Tb1–O11$^{(i)}$	137.85(19)	O12–Tb1–O14$^{(i)}$	70.74(14)
O11$^{(i)}$–Tb1–O12	78.94(14)	O12$^{(i)}$–Tb1–O14	70.74(14)
O11–Tb1–O12	115.08(16)	O12–Tb1–O14	144.32(13)
O11$^{(i)}$–Tb1–O12$^{(i)}$	115.08(16)	O12$^{(i)}$–Tb1–O14$^{(i)}$	144.32(13)
O11–Tb1–O12$^{(i)}$	78.94(14)	O13$^{(i)}$–Tb1–O12$^{(i)}$	72.49(13)
O11–Tb1–O13$^{(i)}$	145.26(13)	O13–Tb1–O12	72.49(13)
O11$^{(i)}$–Tb1–O13	145.26(13)	O13–Tb1–O12$^{(i)}$	79.18(15)
O11$^{(i)}$–Tb1–O13$^{(i)}$	73.91(14)	O13$^{(i)}$–Tb1–O12	79.17(15)
O11–Tb1–O13	73.91(14)	O13$^{(i)}$–Tb1–O13	81.6(2)
O11–Tb1–O14$^{(i)}$	71.61(14)	O13–Tb1–O14	141.52(13)
O11–Tb1–O14	77.17(14)	O13–Tb1–O14$^{(i)}$	110.44(14)
O11$^{(i)}$–Tb1–O14	71.61(14)	O13$^{(i)}$–Tb1–O14	110.44(14)
O11$^{(i)}$–Tb1–O14$^{(i)}$	77.17(14)	O13$^{(i)}$–Tb1–O14$^{(i)}$	141.52(13)
O12–Tb1–O12$^{(i)}$	142.35(19)	O14$^{(i)}$–Tb1–O14	83.25(19)

Symmetry code: (i) *x*, -*y*+3/2, -*z*+1/2.

Table S4. Selected bond angles (ω, deg.) for **DyV_2**.

Angle	ω	Angle	ω
O12–Dy1–O12$^{(i)}$	137.8(2)	O13–Dy1–O14	70.85(16)
O12–Dy1–O13$^{(i)}$	76.68(17)	O13$^{(i)}$–Dy1–O14	144.65(16)
O12$^{(i)}$–Dy1–O13$^{(i)}$	72.05(16)	O13–Dy1–O14$^{(i)}$	144.65(16)
O12$^{(i)}$–Dy1–O13	76.68(17)	O13$^{(i)}$–Dy1–O14$^{(i)}$	70.85(16)
O12–Dy1–O13	72.05(16)	O14–Dy1–O14$^{(i)}$	141.9(2)
O12$^{(i)}$–Dy1–O14	78.76(16)	O11–Dy1–O13	141.28(15)
O12–Dy1–O14$^{(i)}$	78.76(16)	O11$^{(i)}$–Dy1–O13	110.82(16)
O12$^{(i)}$–Dy1–O14$^{(i)}$	115.45(17)	O11–Dy1–O13$^{(i)}$	110.83(16)
O12–Dy1–O14	115.45(17)	O11$^{(i)}$–Dy1–O13$^{(i)}$	141.28(15)
O12$^{(i)}$–Dy1–O11$^{(i)}$	145.07(16)	O11–Dy1–O14	78.88(17)
O12–Dy1–O11	145.07(16)	O11–Dy1–O14$^{(i)}$	72.41(16)
O12–Dy1–O11$^{(i)}$	74.16(16)	O11$^{(i)}$–Dy1–O14	72.41(16)
O12$^{(i)}$–Dy1–O11	74.17(16)	O11$^{(i)}$–Dy1–O14$^{(i)}$	78.88(17)
O13–Dy1–O13$^{(i)}$	83.2(2)	O11–Dy1–O11$^{(i)}$	81.2(2)

Symmetry code: (i) *x*, -*y*+1/2, -*z*+3/2.

Table S5. Hydrogen bonding parameters of structure **GdV_2**.

Fragment D–H···A	Distance/ Å			D–H···A /°
	D–H	H···A	D···A	
O11–H···O6$^{(i)}$	0.85	1.83	2.684(7)	180
O11–H*a*···O3	0.85	2.03	2.821(7)	156
O1–H1*a*···O1S$^{(ii)}$	0.98	1.62	2.602(12)	174
O1–H1*b*···O4A$^{(ii)}$	0.98	2.28	2.98(2)	127
O14–H*b*···O4A$^{(ii)}$	0.85	1.90	2.69(3)	155
O14–H*c*···O7	0.85	1.97	2.726(6)	147
O13–H*d*···O10$^{(iii)}$	0.85	1.89	2.739(7)	180
O13–H*e*···O5$^{(i)}$	0.85	2.02	2.768(7)	147
O12–H*f*···O9$^{(iii)}$	0.85	1.87	2.720(7)	179
O12–H*g*···O8$^{(ii)}$	0.85	1.99	2.785(7)	155

Symmetry codes: ^{i} –1/2+x, y, 1–z; ^{ii} x, 3/2–y, 1/2–z; ^{iii} –1/2+x, 3/2–y, –1/2+z.

Table S6. Hydrogen bonding parameters of structure **TbV_2**.

Fragment D–H···A	Distance/ Å			D–H···A /°
	D–H	H···A	D···A	
O1–H1*a*···O1S$^{(i)}$	0.85	1.79	2.581(14)	154
O1–H1*b*···O4A$^{(ii)}$	0.85	2.12	2.920(10)	156
O11–H11*e*···O6$^{(iii)}$	0.85	1.84	2.686(6)	176
O11–H11*f*···O3	0.85	2.02	2.812(6)	155
O12–H12*e*··O9$^{(iv)}$	0.85	1.88	2.716(6)	168
O12–H12*f*···O8A$^{(ii)}$	0.85	1.97	2.808(8)	170
O13–H13*e*···O8$^{(iv)}$	0.85	1.89	2.742(6)	178
O13–H13*f*···O5$^{(iii)}$	0.85	1.94	2.765(4)	164
O14–H14*g*···O4A$^{(ii)}$	0.86	1.96	2.685(10)	141
O14–H14*h*···O7	0.86	1.89	2.731(6)	165

Symmetry codes: ^{i} 1/2+x, y, 1–z; ^{ii} x, 3/2–y, 1/2–z; ^{iii} –1/2+x, y, 1–z; ^{iv} –1/2+x, 3/2–y, –1/2+z.

Table S7. Hydrogen bonding parameters of structure **DyV_2**.

Fragment D–H···A	Distance/ Å			D–H···A /°
	D–H	H···A	D···A	
O1–H1*a*···O1S$^{(i)}$	0.86	1.80	2.593(16)	154
O1–H1*b*···O6A$^{(ii)}$	0.86	2.13	2.96(3)	162
O11–H11*e*···O8$^{(iii)}$	0.85	1.89	2.738(8)	180
O11–H11*f*···O3$^{(iv)}$	0.85	2.02	2.768(7)	147
O12–H12*e*···O4$^{(iii)}$	0.85	1.83	2.679(8)	180
O12–H12*f*···O5	0.85	2.03	2.824(7)	156
O13–H13*e*···O6A	0.85	2.02	2.71(3)	137
O13–H13*f*···O5$^{(ii)}$	0.85	2.54	3.346(7)	158
O14–H14*g*···O7$^{(iv)}$	0.85	1.86	2.713(7)	180
O14–H14*h*···O10$^{(ii)}$	0.85	1.99	2.782(8)	155

Symmetry codes: ^{i} 1/2+x, 1/2–y, –1/2+z; ^{ii} x, 1/2–y, 3/2–z; ^{iii} –1/2+x, y, 1–z; ^{iv} –1/2+x, 1/2–y, 1/2+z.

Magnetic properties

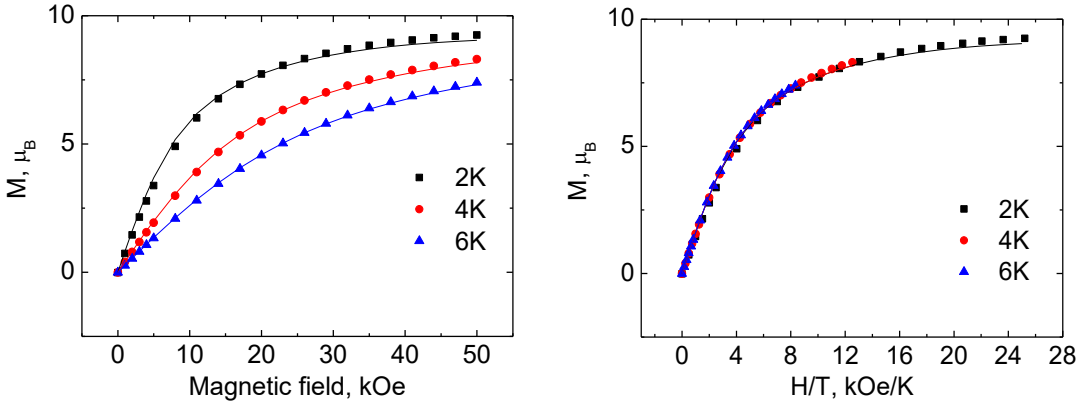

Figure S9. Dependencies of the magnetization [μ_B] *vs dc*-magnetic field H (left) and H/T (right) for **GdV_2** at 2, 4 and 6 K. Calculated values are represented by black lines.

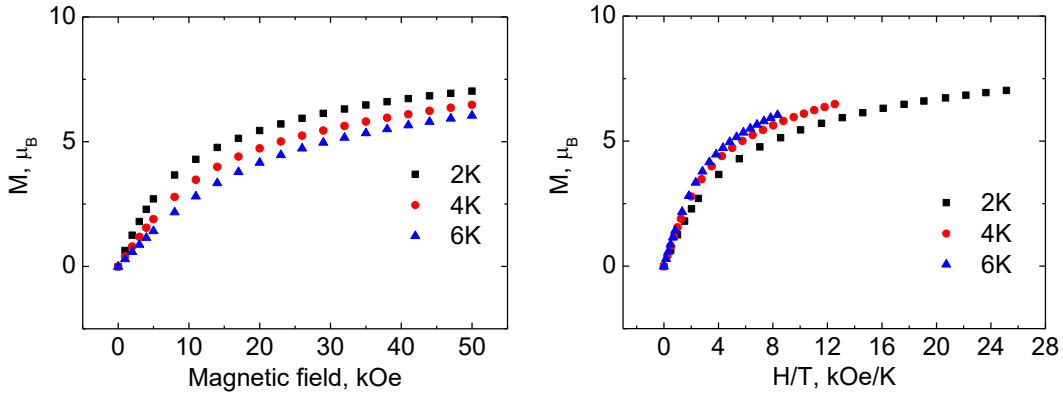

Figure S10. Dependencies of the magnetization [μ_B] *vs dc*-magnetic field H (left) and H/T (right) for **TbV_2** at 2, 4 and 6 K.

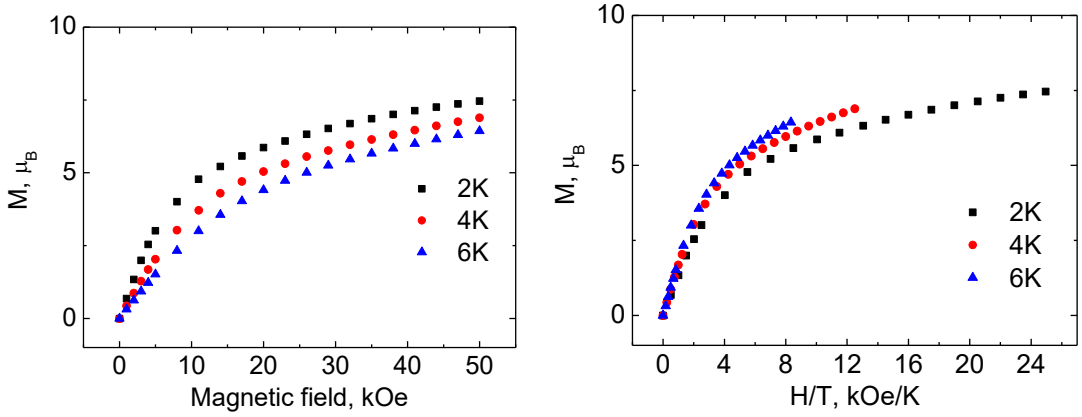

Figure S11. Dependencies of the magnetization [μ_B] *vs dc*-magnetic field H (left) and H/T (right) for **DyV_2** at 2, 4 and 6 K.

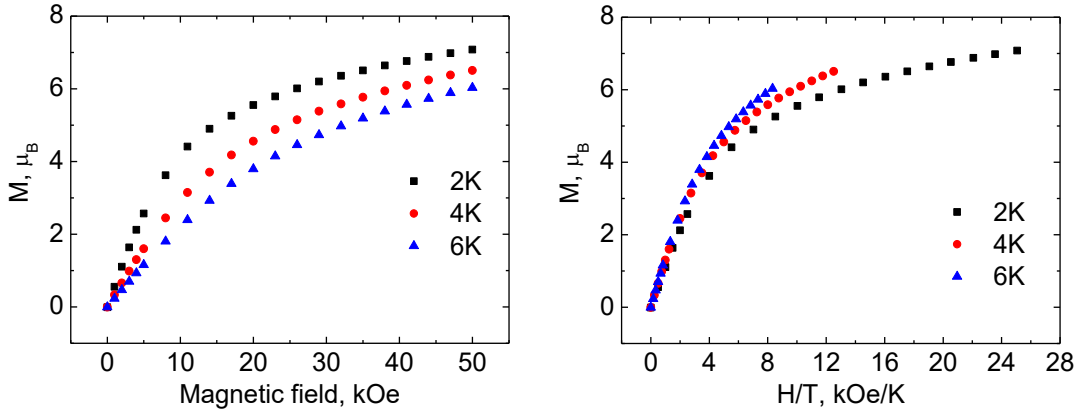

Figure S12. Dependencies of the magnetization [μ_B] *vs dc*-magnetic field H (left) and H/T (right) for **ErV$_2$** at 2, 4 and 6 K.

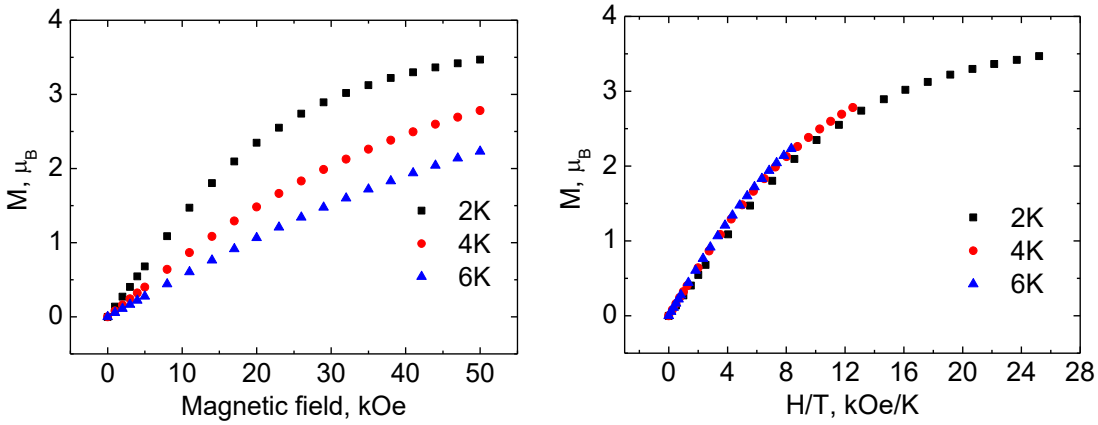

Figure S13. Dependencies of the magnetization [μ_B] *vs dc*-magnetic field H (left) and H/T (right) for **YbV$_2$** at 2, 4 and 6 K.

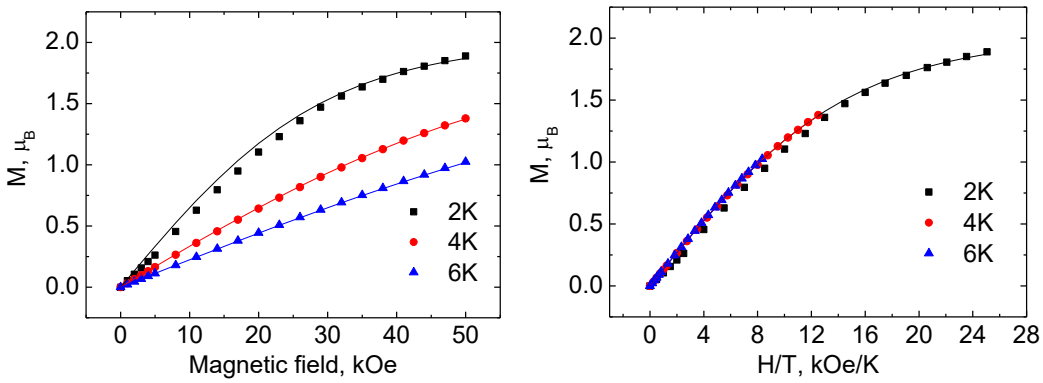

Figure S14. Dependencies of the magnetization [μ_B] *vs dc*-magnetic field H (left) and H/T (right) for **LuV$_2$** at 2, 4 and 6 K. Calculated values are represented by black lines.

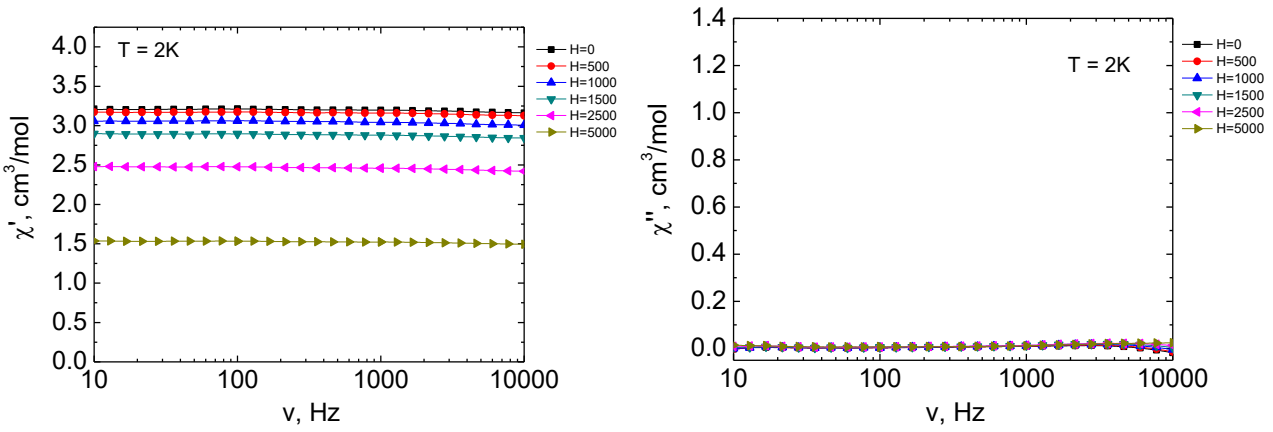

Figure S15. Frequency dependencies of the in-phase (χ', left) and out-of-phase (χ", right) components of the ac susceptibility for **TbV_2** up to a 5000 Oe dc magnetic field at 2 K.

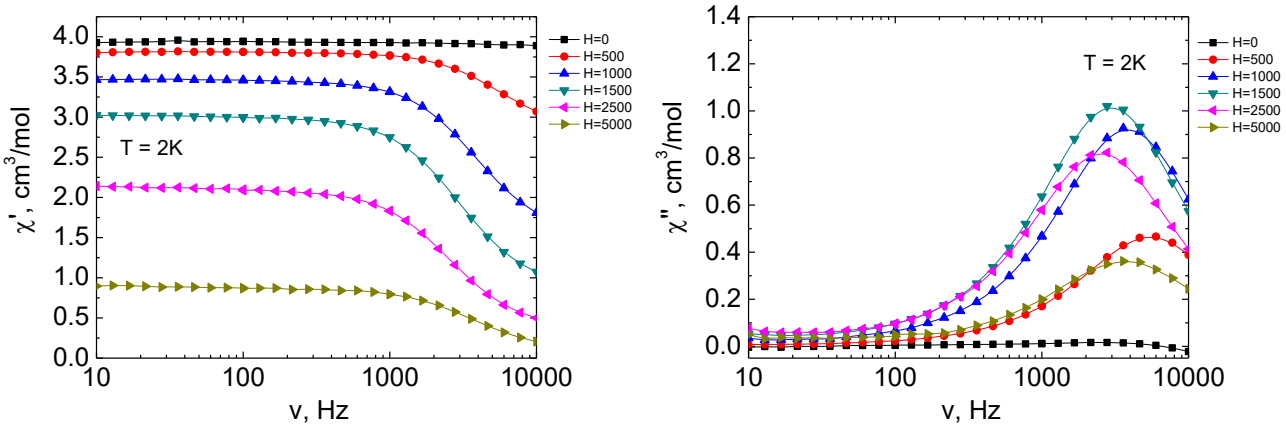

Figure S16. Frequency dependencies of the in-phase (χ', left) and out-of-phase (χ", right) components of the ac susceptibility for **GdV_2** up to a 5000 Oe dc magnetic field at 2 K.

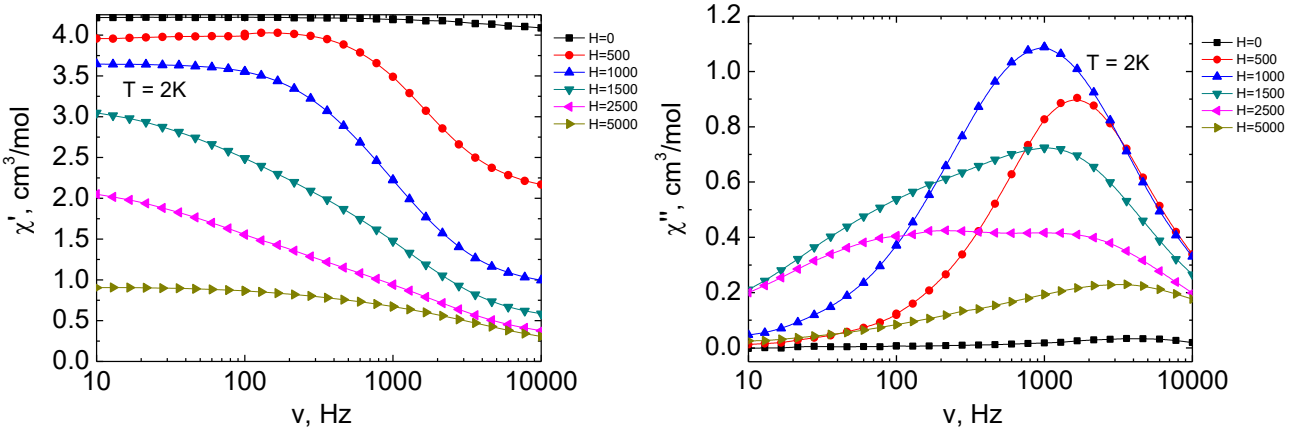

Figure S17. Frequency dependencies of the in-phase (χ', left) and out-of-phase (χ", right) components of the ac susceptibility for **DyV_2** up to a 5000 Oe dc magnetic field at 2 K.

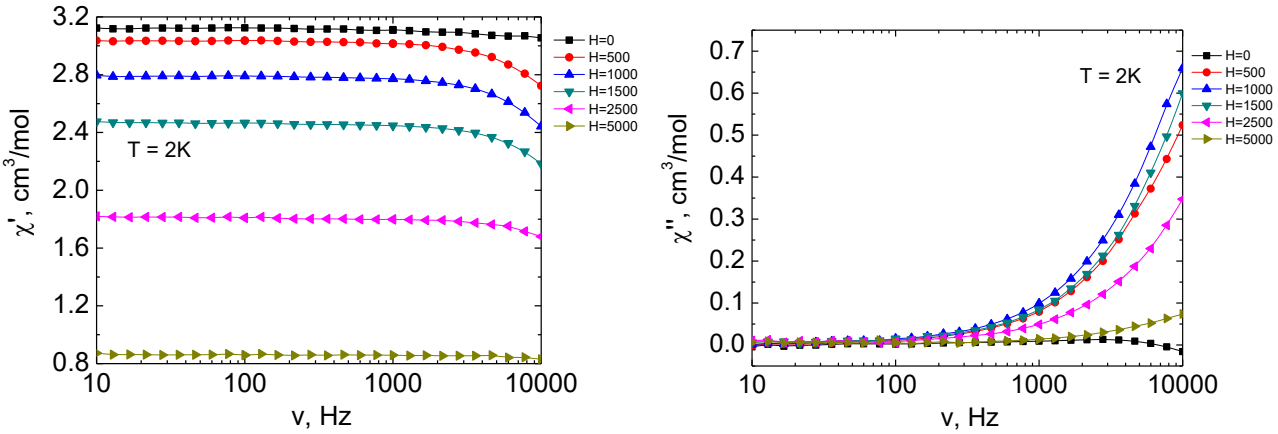

Figure S18. Frequency dependencies of the in-phase (χ', left) and out-of-phase (χ", right) components of the ac susceptibility for **ErV₂** up to a 5000 Oe dc magnetic field at 2 K.

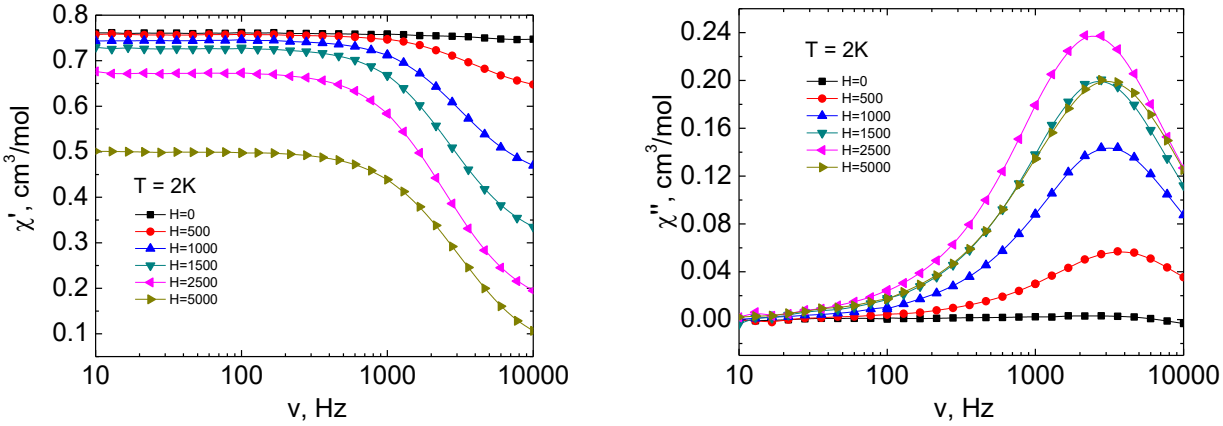

Figure S19. Frequency dependencies of the in-phase (χ', left) and out-of-phase (χ", right) components of the ac susceptibility for **YbV₂** up to a 5000 Oe dc magnetic field at 2 K.

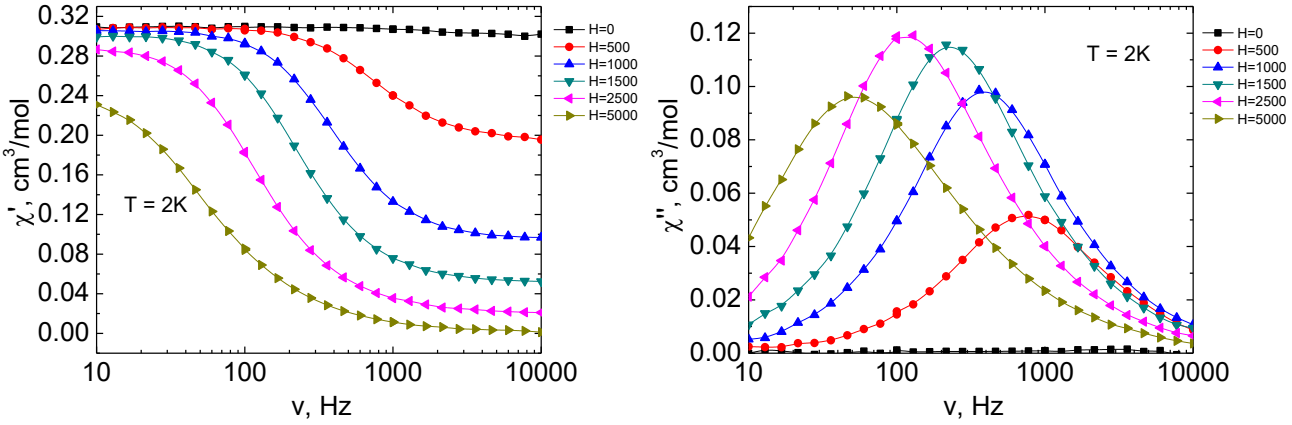

Figure S20. Frequency dependencies of the in-phase (χ', left) and out-of-phase (χ", right) components of the ac susceptibility for **LuV₂** up to a 5000 Oe dc magnetic field at 2 K.

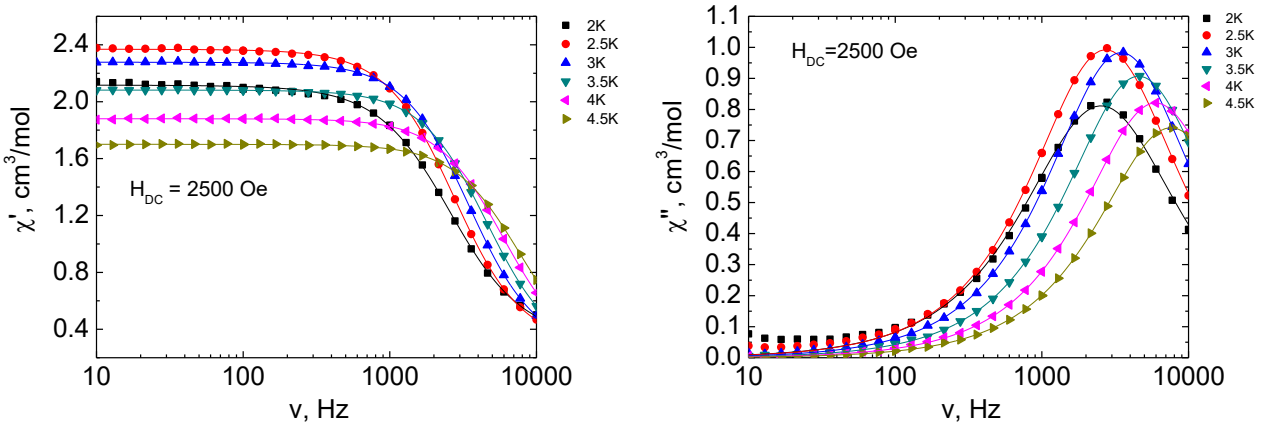

Figure S21. Frequency dependences of the in-phase (χ', left) and out-of-phase (χ", right) components of ac magnetic susceptibility for **GdV_2** in the temperature range of 2-4.5 K under a 2500 Oe dc magnetic field. Solid lines represent fitting by the generalized Debye model.

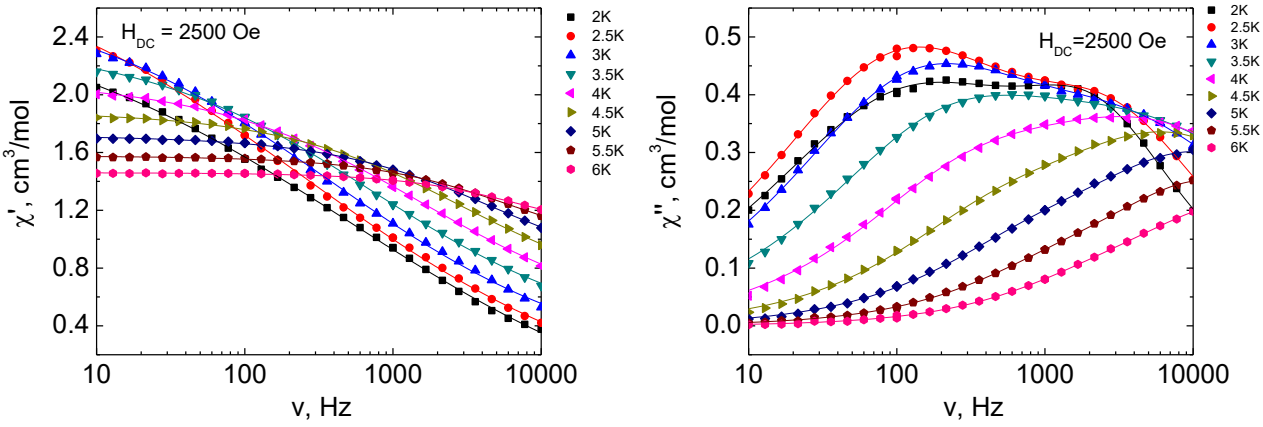

Figure S22. Frequency dependences of the in-phase (χ', left) and out-of-phase (χ", right) components of ac magnetic susceptibility for **DyV_2** in the temperature range of 2-6 K under a 2500 Oe dc magnetic field. Solid lines represent fitting by the generalized Debye model.

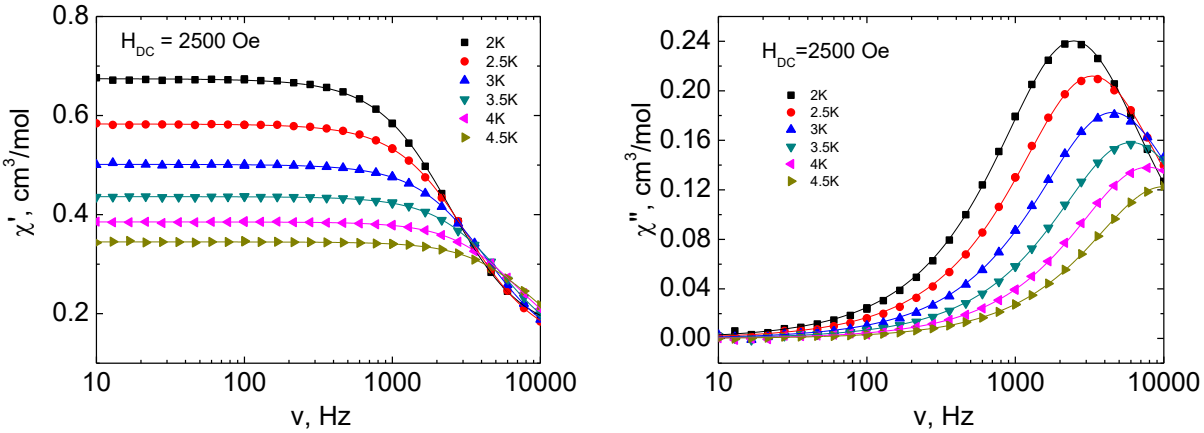

Figure S23. Frequency dependences of the in-phase (χ', left) and out-of-phase (χ", right) components of ac magnetic susceptibility for **YbV_2** in the temperature range of 2-4.5 K under a 2500 Oe dc magnetic field. Solid lines represent fitting by the generalized Debye model.

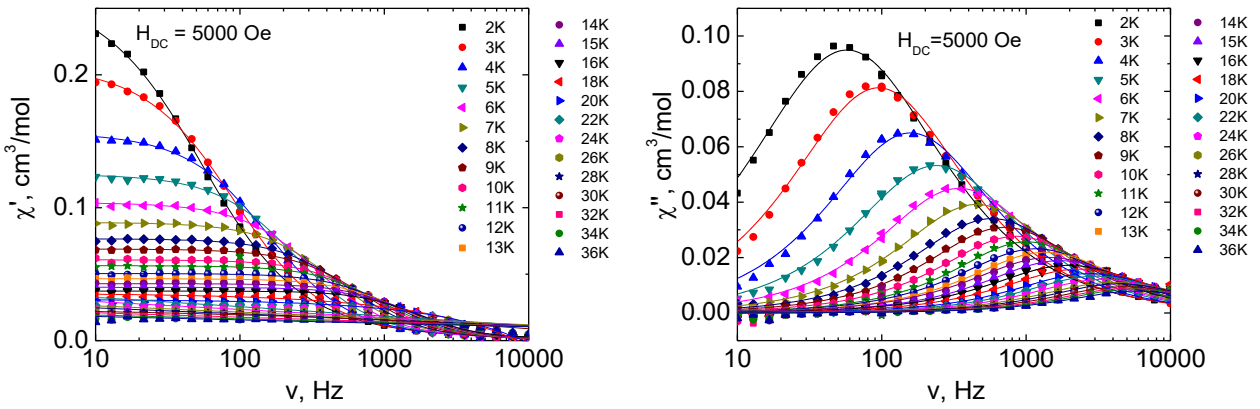

Figure S24. Frequency dependences of the in-phase (χ', left) and out-of-phase (χ'') components of ac magnetic susceptibility for **LuV_2** in the temperature range of 2-36 K under a 5000 Oe dc magnetic field. Solid lines represent fitting by the generalized Debye model.

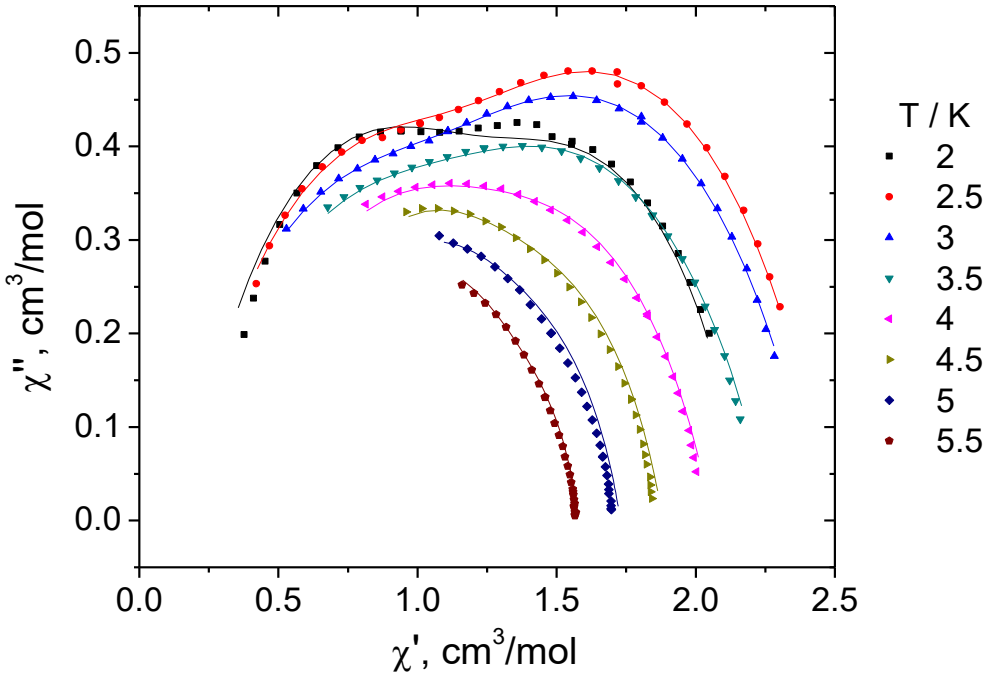

Figure S25. Cole-Cole plots for **DyV_2**. Solid lines were fitted by generalized Debye model for two modes of relaxation.

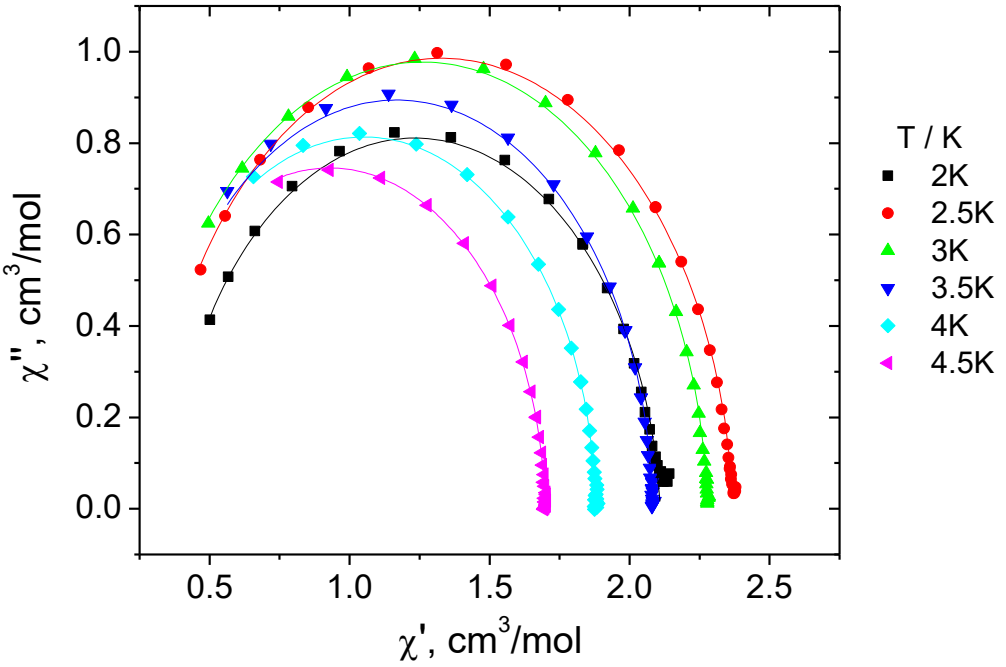

Figure S26. Cole-Cole plots for **GdV$_2$**. Solid lines were fitted by generalized Debye model.

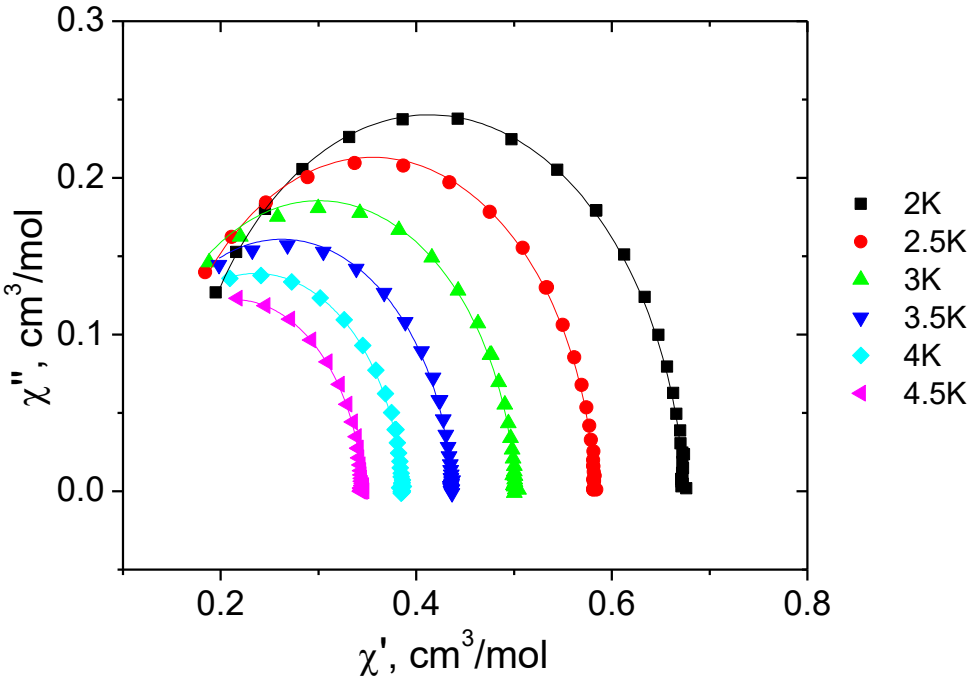

Figure S27. Cole-Cole plots for **YbV$_2$**. Solid lines were fitted by generalized Debye model.

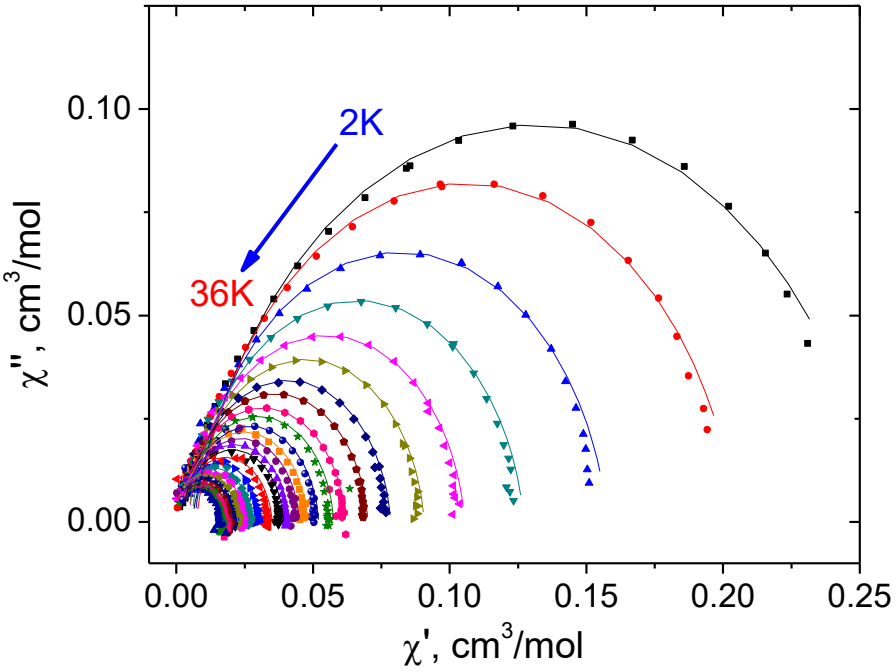

Figure S28. Cole-Cole plots for **LuV₂**. Solid lines were fitted by generalized Debye.

Table S8. Fitting of the τ *vs.* T dependences for **GdV₂** under an optimal dc field (H_{DC} = 2500 Oe, T = 4.5 K). Meaningless parameters are specified in red color while yellow color emphasizes insufficient R^2 values. Reliable fits are specified in green color.

Fitting	Fit function, temperature range, best-fit parameters with uncertainties.
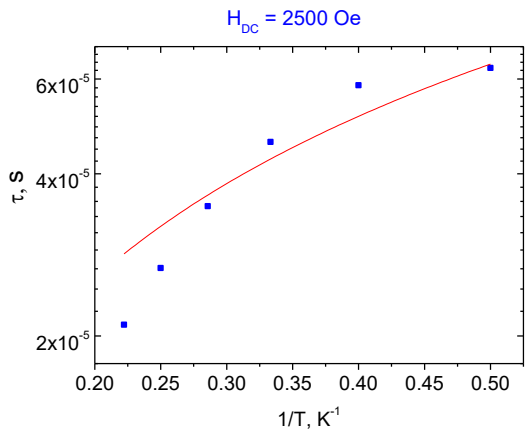	**Direct** $\tau^{-1} = A_{direct}TH^4$ $A_{direct} = 2.0 \cdot 10^{-10} \pm 1 \cdot 10^{-11}$ $K^{-1}Oe^{-4}s^{-1}$ $R^2 = 0.89654$

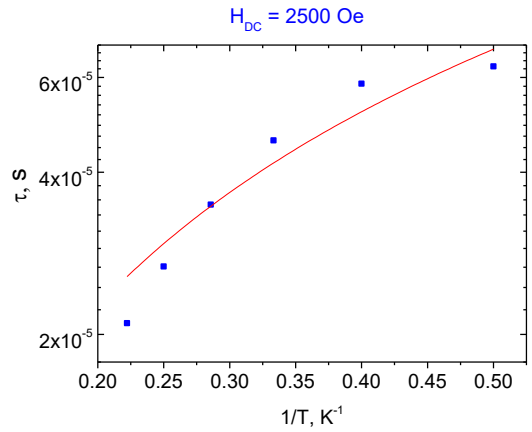	**Raman** $\tau^{-1} = C_{Raman} T^{n\_Raman}$ C_{Raman}=6435 ± 1199 $s^{-1}K^{-nRaman}$ n_{Raman}=1.2 ± 0.2 R^2 = 0.90196
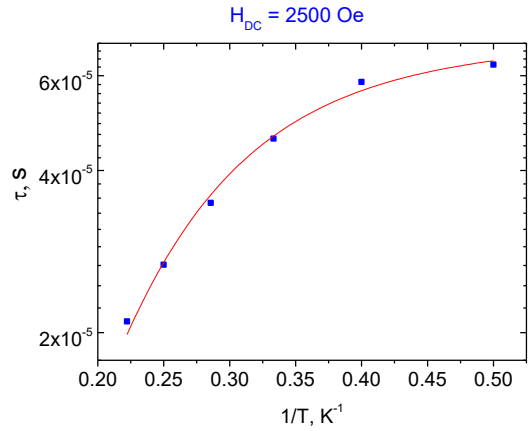	**Raman + QTM** $\tau^{-1} = C_{Raman} T^{nRaman} + B$ C_{Raman}= 104 ± 76$s^{-1}K^{-nRaman}$ n_{Raman}= 3.9 ± 0.5 B = 14099 ± 859 s^{-1} R^2 = 0.99394
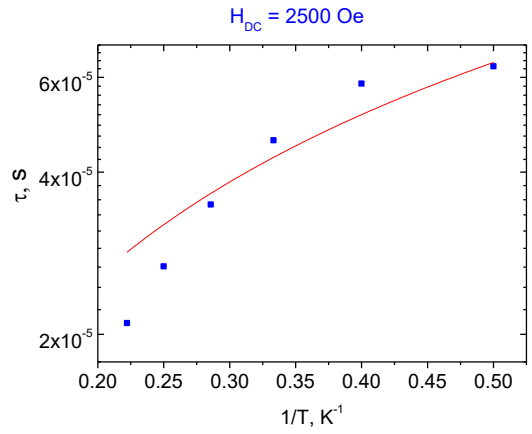	**Direct + QTM** $\tau^{-1} = A_{direct} T H^4 + B$ B = 0 ± 4505 s^{-1} A_{direct} = 2.0·10^{-10} ± 5·10^{-11} $K^{-1}Oe^{-4}s^{-1}$ R^2 = 0.87069
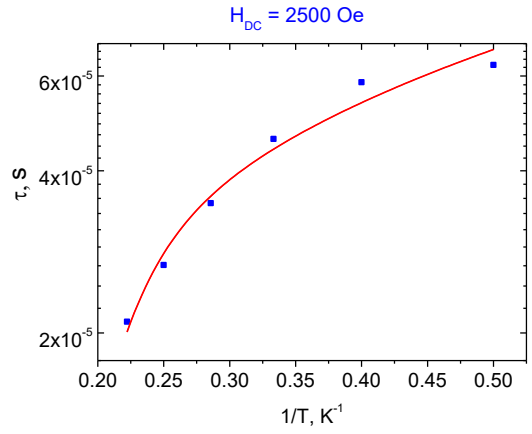	**Raman + Direct** $\tau^{-1} = C_{Raman} T^{nRaman} + A_{direct} T H^4$ C_{Raman}= 0.0374 ± 0.3866 $s^{-1}K^{-nRaman}$ n_{Raman}=9 ± 7 A_{direct} = 1.9·10^{-10} ± 1·10^{-11} $K^{-1}Oe^{-4}s^{-1}$ R^2 = 0.94244

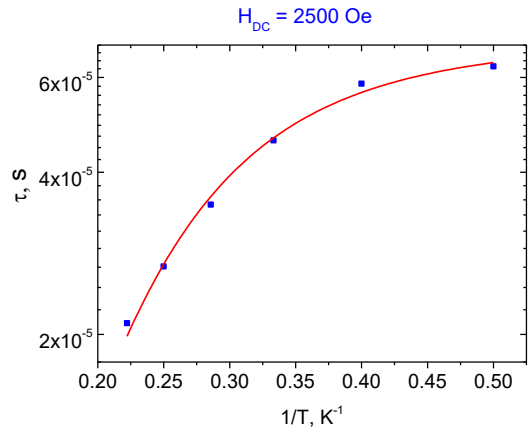

Raman + Direct + QTM

$\tau^{-1} = C_{Raman}T^{nRaman} + A_{direct}TH^4 + B$

$C_{Raman} = 103 \pm 24036$ $s^{-1}K^{-nRaman}$

$n_{Raman} = 4 \pm 6$

$A_{direct} = 0 \pm 3.4 \cdot 10^{-6}$ $K^{-1}Oe^{-4}s^{-1}$

$B = 14101 \pm 3$ s^{-1}

$R^2 = 0.98484$

Quantum chemical calculations

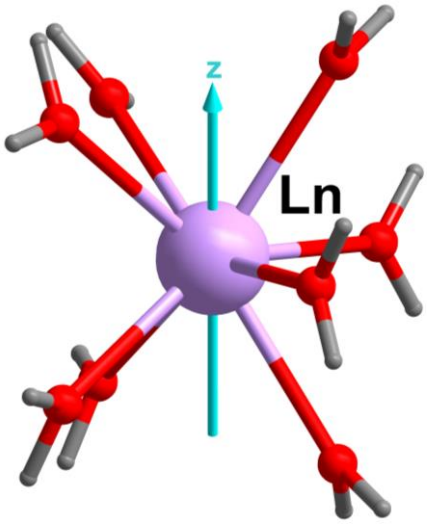

Fig. S29. CASSCF computed main magnetic g_{zz}-axis of the $[Ln(H_2O)_8]^{3+}$ unit.

Table S9. Calculated energy (cm^{-1}) and wavefunction decomposition of Ising pseudo-doublets analysis for Tb^{3+} ion in **TbV_2** (values above 10% are given, the major dominating values are kept in bold).

Energy	Wavefunction decomposition
0.000	**99.2%|±6⟩**
0.003	**99.2%|±6⟩**
140.265	**24.8%|±2⟩**+24.4%|±3⟩+20.2%|±5⟩+16.0%|±1⟩+13.2%|±4⟩
140.641	**27.8%|±2⟩**+25.0%|±3⟩+21.2%|±5⟩+13.4%|±4⟩+10.4%|±1⟩
165.817	**30.4%|±5⟩**+29.4%|±1⟩+24.9%|0⟩
168.916	**38.8%|±5⟩**+34.0%|±1⟩+15.6%|±2⟩

182.405	**45.9%|0⟩**+26.6%|±5⟩+14.0%|±2⟩
190.398	**30.0%|±1⟩**+27.4%|±5⟩+22.8%|±3⟩
202.445	**19.8%|±3⟩**+14.8%|0⟩+12.4%|±5⟩+10.8%|±4⟩
228.104	**34.0%|±4⟩**+33.2%|±2⟩+14.6%|±1⟩
231.669	**39.8%|±2⟩**+30.2%|±4⟩+16.8%|±1⟩
307.092	**40.8%|±3⟩**+37.6%|±4⟩+13.6%|±2⟩
307.355	**41.2%|±3⟩**+36.3%|±4⟩+14.6%|±2⟩

Table S10. Calculated energy (cm^{-1}) and g-tensors for each Kramers doublets for Ln^{3+} ions in compounds **LnV_2**.

$\|\pm M_J\rangle$ states	Energy	g_{xx}	g_{yy}	g_{zz}
Dy^{3+}				
KD^0	0	0.007	0.014	19.435
KD^1	105.750	0.061	0.067	15.456
KD^2	148.741	2.311	2.717	11.722
KD^3	195.362	7.078	6.248	2.415
KD^4	245.444	2.431	3.522	9.573
KD^5	286.940	1.200	2.359	13.685
KD^6	326.751	0.550	0.787	18.207
KD^7	364.813	0.289	0.436	19.245
Er^{3+}				
KD^0	0	0.742	2.677	14.920
KD^1	45.371	8.633	5.993	2.363
KD^2	80.548	1.864	2.272	8.841
KD^3	113.082	0.288	0.525	16.203
KD^4	156.289	2.739	2.510	0.427
KD^5	164.351	6.639	3.914	0.775
KD^6	203.100	0.080	0.836	9.742
KD^7	255.670	0.015	0.148	15.846
Yb^{3+}				
KD^0	0	0.144	0.455	7.618
KD^1	109.280	1.283	1.974	6.213
KD^2	220.175	1.693	2.507	4.777
KD^3	282.596	0.233	0.296	7.909

Table S11. Calculated energy (cm^{-1}) and wavefunction decomposition analysis of doublets for Dy^{3+}, Er^{3+}, and Yb^{3+} ions in compounds **LnV_2** (values above 10% are given, the major dominating values are kept in bold).

$\|\pm M_J\rangle$ states	Energy	Wavefunction decomposition
Dy^{3+}		
1	0	**93.8%|±15/2⟩**
2	105.750	**74.0%|±13/2⟩**+10.8%|±7/2⟩
3	148.741	**41.5%|±11/2⟩**+18.5%|±5/2⟩+16.0%|±3/2⟩+10.5%|±9/2⟩
4	195.362	**34.6%|±9/2⟩**+25.0%|±11/2⟩+17.1%|±1/2⟩+15.2%|±3/2⟩
5	245.444	**30.7%|±7/2⟩** + 30.1%|±9/2⟩ + 21.7%|±1/2⟩ + 13.3%|±5/2⟩
6	286.940	**31.7%|±7/2⟩** + 30.5%|±5/2⟩ + 26.9%|±3/2⟩
7	326.751	**26.9%|±11/2⟩** + 19.1%|±9/2⟩ + 18.4%|±5/2⟩ + 17.3%|±13/2⟩
8	364.813	**45.4%|±1/2⟩** + 33.4%|±3/2⟩ + 12.6%|±5/2⟩
Er^{3+}		
1	0	**66.2%|±15/2⟩** + 18.1%|±11/2⟩
2	45.371	**32.4%|±13/2⟩** + 28.4%|±5/2⟩ + 13.3%|±1/2⟩ + 10.0%|±3/2⟩
3	80.548	**24.8%|±3/2⟩** + 23.4%|±13/2⟩ + 14.4%|±9/2⟩ + 10.7%|±5/2⟩
4	113.082	**37.0%|±1/2⟩** + 16.6%|±9/2⟩ + 16.5%|±3/2⟩ + 11.9%|±5/2⟩+ 11.2%|±7/2⟩
5	156.289	**23.2%|±1/2⟩** + 22.7%|±9/2⟩ + 15.4%|±11/2⟩ + 10.7%|±15/2⟩ + 10.6%|±13/2⟩
6	164.351	**48.3%|±7/2⟩** + 16.3%|±11/2⟩ + 13.7%|±3/2⟩
7	203.100	**30.2%|±11/2⟩** + 20.8%|±13/2⟩ + 18.8%|±5/2⟩ + 12.4%|±9/2⟩
8	255.670	**19.4%|±5/2⟩** + 19.2%|±3/2⟩ + 15.1%|±1/2⟩ + 12.0%|±7/2⟩ + 11.0%|±9/2⟩
Yb^{3+}		
1	0	**49.2%|±7/2⟩** + 27.1%|±3/2⟩ + 22.4%|±5/2⟩
2	109.280	**44.4%|±5/2⟩** + 37.8%|±1/2⟩ + 13.6%|±3/2⟩
3	220.175	**38.2%|±3/2⟩** + 23.0%|±7/2⟩ + 22.9%|±1/2⟩ + 15.9%|±5/2⟩
4	282.596	**37.9%|±1/2⟩** + 23.6%|±7/2⟩ + 21.1%|±3/2⟩ + 17.3%|±5/2⟩

Table S12. Calculated crystal-field parameters B_k^q (cm^{-1}) for nonequivalent Ln^{3+} ions in compounds **LnV_2**. The major components in the table are in bold.

k	q	B			
		Tb^{3+}	Dy^{3+}	Er^{3+}	Yb^{3+}
2	–2	–0.638	$-0.846\cdot10^{-3}$	**0.725**	$-0.457\cdot10^{-3}$
	–1	$\mathbf{0.322\cdot10^{1}}$	$-0.107\cdot10^{-2}$	$-0.852\cdot10^{-4}$	$-0.490\cdot10^{-3}$
	0	$-0.147\cdot10^{1}$	–0.139	–0.391	$-0.192\cdot10$
	1	–0.989	**–0.750**	$-0.126\cdot10^{-3}$	$0.615\cdot10$
	2	0.306	–0.566	$-0.783\cdot10^{-1}$	**0.923·10**
4	–4	$-0.166\cdot10^{-3}$	$0.489\cdot10^{-4}$	$-0.176\cdot10^{-2}$	$-0.164\cdot10^{-4}$
	–3	$0.998\cdot10^{-2}$	$-0.213\cdot10^{-3}$	$-0.264\cdot10^{-6}$	$-0.479\cdot10^{-4}$
	–2	$-0.116\cdot10^{-1}$	$0.454\cdot10^{-4}$	$-0.122\cdot10^{-2}$	$-0.507\cdot10^{-4}$
	–1	$\mathbf{-0.325\cdot10^{-1}}$	$-0.162\cdot10^{-4}$	$-0.314\cdot10^{-6}$	$-0.333\cdot10^{-4}$
	0	$-0.123\cdot10^{-1}$	$-0.222\cdot10^{-2}$	$-0.196\cdot10^{-2}$	$0.242\cdot10^{-1}$
	1	$0.894\cdot10^{-2}$	$-0.161\cdot10^{-1}$	$0.104\cdot10^{-5}$	**0.585**
	2	$0.317\cdot10^{-2}$	$0.206\cdot10^{-1}$	$0.120\cdot10^{-1}$	0.349
	3	$0.330\cdot10^{-2}$	$\mathbf{-0.584\cdot10^{-1}}$	$0.287\cdot10^{-5}$	0.454
	4	$0.987\cdot10^{-3}$	$0.979\cdot10^{-2}$	$\mathbf{-0.175\cdot10^{-1}}$	$0.145\cdot10^{-1}$
6	–6	$-0.133\cdot10^{-4}$	$-0.751\cdot10^{-6}$	$-0.253\cdot10^{-4}$	$0.529\cdot10^{-6}$
	–5	$-0.272\cdot10^{-4}$	$-0.196\cdot10^{-5}$	$-0.306\cdot10^{-6}$	$0.386\cdot10^{-5}$
	–4	$0.128\cdot10^{-4}$	$0.901\cdot10^{-6}$	$0.115\cdot10^{-3}$	$-0.265\cdot10^{-6}$
	–3	$-0.104\cdot10^{-3}$	$-0.107\cdot10^{-5}$	$-0.902\cdot10^{-7}$	$-0.465\cdot10^{-5}$
	–2	$0.394\cdot10^{-4}$	$0.110\cdot10^{-6}$	$0.663\cdot10^{-4}$	$-0.151\cdot10^{-5}$
	–1	$\mathbf{-0.170\cdot10^{-3}}$	$0.105\cdot10^{-6}$	$0.739\cdot10^{-7}$	$-0.914\cdot10^{-6}$
	0	$-0.180\cdot10^{-4}$	$-0.111\cdot10^{-4}$	$-0.436\cdot10^{-5}$	$-0.654\cdot10^{-3}$
	1	$0.241\cdot10^{-4}$	$0.138\cdot10^{-3}$	$-0.264\cdot10^{-7}$	$0.175\cdot10^{-1}$
	2	$0.378\cdot10^{-4}$	$0.722\cdot10^{-5}$	$0.163\cdot10^{-3}$	$0.939\cdot10^{-2}$
	3	$0.556\cdot10^{-4}$	$-0.186\cdot10^{-3}$	$-0.162\cdot10^{-6}$	$\mathbf{0.328\cdot10^{-1}}$
	4	$-0.117\cdot10^{-3}$	$0.191\cdot10^{-3}$	$\mathbf{-0.334\cdot10^{-3}}$	$-0.163\cdot10^{-2}$
	5	$0.160\cdot10^{-3}$	$\mathbf{-0.457\cdot10^{-3}}$	$-0.753\cdot10^{-7}$	$-0.120\cdot10^{-1}$
	6	$-0.305\cdot10^{-5}$	$-0.109\cdot10^{-3}$	$0.280\cdot10^{-3}$	$0.240\cdot10^{-3}$